



HAL
open science

On the failure of classic elasticity in predicting elastic wave propagation in gyroid lattices for very long wavelengths

Giuseppe Rosi, Nicolas Auffray, Christelle Combescure

► **To cite this version:**

Giuseppe Rosi, Nicolas Auffray, Christelle Combescure. On the failure of classic elasticity in predicting elastic wave propagation in gyroid lattices for very long wavelengths. *Symmetry*, 2020. hal-02800649v1

HAL Id: hal-02800649

<https://hal.science/hal-02800649v1>

Submitted on 5 Jun 2020 (v1), last revised 23 Jun 2020 (v2)

HAL is a multi-disciplinary open access archive for the deposit and dissemination of scientific research documents, whether they are published or not. The documents may come from teaching and research institutions in France or abroad, or from public or private research centers.

L'archive ouverte pluridisciplinaire **HAL**, est destinée au dépôt et à la diffusion de documents scientifiques de niveau recherche, publiés ou non, émanant des établissements d'enseignement et de recherche français ou étrangers, des laboratoires publics ou privés.

Article

On the failure of classic elasticity in predicting elastic wave propagation in gyroid lattices for very long wavelengths

Giuseppe Rosi ¹ , Nicolas Auffray², Christelle Combescure²

¹ Univ Paris Est Creteil, CNRS, MSME, F-94010 Creteil, France; giuseppe.rosi@u-pec.fr.

² Univ Gustave Eiffel, CNRS, MSME, F-77447 Marne-la-Vallée, France.

Version June 5, 2020 submitted to *Symmetry*

Abstract: In this work we investigate the properties of elastic waves propagating in gyroid lattices. First, we rigorously characterize the lattice from the point of view of crystallography. Second, we use Bloch-Floquet analysis to compute the dispersion relations for elastic waves. The results for very long wavelengths are then compared to those given by classic elasticity for a cubic material. A discrepancy is found in terms of the polarization of waves and it is related to the noncentrosymmetry of the gyroid. The gyroid lattice results to be acoustically active, meaning that transverse waves exhibit a circular polarization when they propagate along an axis of rotational symmetry. This phenomenon is present even for very long wavelengths and it is not captured by classic elasticity.

Keywords: elastic waves, noncentrosymmetry, gyroid, crystallography, chirality

1. Introduction

Architected materials are those that possess an inner geometry [1]. This multi-scale spatial arrangement of the constitutive materials allows for achieving mechanical properties that are not present in the bulk material itself [2]. Although this appears to be an engineering-based approach to materials design, it should be noted that this strategy is, in fact, central in nature where biomaterials must perform many functions from a small and limited set of elementary chemical elements [3,4]. Therefore, to enhance some target properties, regular patterns often emerge. The best-known example is the honeycomb, where bees need to maximise the volume of the cells while minimizing the quantity of matter (wax) used [5]. Another example is the iridescent color of the wings of some butterflies. This phenomenon is due to the non-centrosymmetric mesostructure of the material constituting the wings which acts a photonic crystal [6,7].

The study of elastic waves propagating in architected materials is of particular interest since unconventional effects due to the local organisation of the matter can emerge at the macroscale. In order to study these phenomena adequately, two points of view can be adopted. Either to describe all the details of the architecture, or to consider an effective continuum as replacement. The first option is very general since no particular modeling assumptions are involved. However, since the inner geometry of the material has to be explicitly described and meshed, the numerical cost is often prohibitive for actual applications. Moreover, the computed solution often contains many unnecessary details for practical use. The second option, which is based on elastodynamic homogenization [8–10] amounts to substitute the initial heterogeneous material by an equivalent homogeneous continuum. This equivalence is only valid under specific assumptions on the range of variation of some intrinsic parameters, and hence more restrictive than the first approach. However, within the validity domain of

32 the method, the physics, up to a certain order¹, is correctly described. This results in a fairly important
33 reduction in the computational cost, which is very interesting for optimizing an architected material,
34 since in that case the numerical model has to be computed many times along the process.

35 For infinite Periodic Architected Materials (PAM), which are the subject of this paper, the
36 condition under which the complete wave problem can be substituted by an effective one relies on the
37 ratio (η) between the size of the periodic unit cell (L) and the wavelength (λ) of the mechanical field.
38 When this ratio approaches zero the classical Long-Wavelength (LW) approximation is obtained and,
39 provided that the frequency ω is also low (Low-Frequency (LF) approximation), the heterogeneous
40 material can be replaced by a classical effective continuum. This situation, which has been well
41 investigated, is completely contained in what is called LF-LW elastodynamics homogenization [8–10].
42 When the equivalent medium is a classical continuum (Cauchy continuum), the effective behavior
43 is non-sensitive to certain features of the inner geometry such as noncentrosymmetry, chirality or
44 $n > 4$ -fold axis of rotational anisotropy [11–13].

45 Now, when the scale separation ratio η is small, but not vanishingly small, elastic waves
46 propagating through the matter interact with the inner architecture. In this situation, several
47 propagation quantities, such as the phase and group velocities, become frequency dependent and the
48 wave propagation is *dispersive* [14]. Non standard dependencies on the architecture, that were left over
49 in LF-LW approximation, may thus appear. These situations, which are outside the frame of standard
50 elastodynamic homogenization, can nevertheless be modeled if the Cauchy equivalent continuum is
51 replaced by a generalized continuum [15–17]. In this work we focus on bulk propagation, however it
52 is important to notice that effects near boundaries, such as surface waves [18,19], are also of particular
53 interest.

54 Wave propagation in non-centrosymmetric or chiral materials, the two concepts being distinct²,
55 has been a subject of interest among physicists for centuries, mainly in the field of optics and
56 electromagnetism. The first experiments showing the interaction of light with chiral molecules
57 like sugar goes back to the beginning of the 19th century [20]. The effect which is associated to
58 electromagnetic waves propagating in non-centrosymmetric crystals is the rotation of the plane of
59 polarization when the wave propagates along an optical axis, i.e. an axis of rotational symmetry. The
60 rotation is due to the decomposition of the linearly polarised transverse wave into two circularly
61 polarised waves with opposite handedness and different phase velocities [21]. This phenomenon is
62 known under the name of "optical activity". The analogue of this effect can be observed for elastic
63 waves, and it is known as "acoustical activity" [21]. It is interesting to remark that optically active
64 crystals are also found to be acoustically active and that, as it will be shown in this paper, this effect
65 can occur also in the LF-LW regime.

66 Recently, the interest in investigating the properties of materials based on chiral and
67 non-centrosymmetric architectures has grown. To this end it is important to point out that chirality
68 and noncentrosymmetry are not equivalent, and that their impact on the physics of the problem can be
69 different.

70 The set of transformations that let the unit cell of an architected material invariant constitutes
71 its symmetry group. The material is said *chiral* if its symmetry group contains only rotations, and it is
72 said to be centrosymmetric when it contains the inversion [22]. It is important to observe that in a 2D
73 space the inversion is a rotation (preserving the material orientation) while, in 3D, it is a transformation
74 reversing the material orientation. Since the nature of the inversion depends on the dimension of the
75 space, the implication between chirality and centrosymmetry are not the same in 2D and 3D. In 2D,

¹ An effective theory is a reduced model obtained by filtering the actual physics so as to retain, in the continuum formulation, only the most prominent effects. Depending on the targeted applications, the effective model can be of different degrees of richness.

² see Appendix A for a dictionary of point groups and their associated properties

76 the chirality and centrosymmetry are independent [15], while in 3D chiral materials are necessarily
 77 non-centrosymmetric [23].

78 Several works can be found in the literature that investigate 2D chiral elasticity, and focus on their
 79 unusual mechanical properties such as negative Poisson ratio [24,25]. Concerning wave propagation,
 80 these architectures have been extensively studied [26–28] and the need for a generalized continuum
 81 theory in order to capture the onset of dispersion and anisotropy at higher frequencies has been
 82 pointed out [15,16]. In all these cases, the unit cells under investigation are chiral and centrosymmetric.
 83 It is worth noting that such a combination is possible uniquely in 2D. When moving to 3D, the picture
 84 becomes more complex, and due to habits coming from the 2D situation, an ambiguity between the two
 85 definitions can be usually found in the literature. For instance, the well-known and studied in-plane
 86 hexachiral and tetrachiral patterns [29,30], are no more chiral once extruded in 3D.

87 Concerning wave propagation in non-centrosymmetric materials, if the phenomenon can be
 88 studied in 2D [15], the effects become even more interesting in 3D as polarization of waves are then
 89 richer. As a consequence, interest in 3D non-centrosymmetric metamaterials have recently emerged for
 90 their stretch-twist coupling [31] or their acoustical activity [32]. The effects related to size dependent
 91 properties and characteristic lengths are also exploited and investigated in [33] and a micropolar
 92 generalized model is used to investigate acoustical activity in [34].

93 In the present work, the features of elastic wave propagation in non-centrosymmetric architected
 94 materials are investigated. Among them, gyroid materials are probably the most commonly used.
 95 In electromagnetics they are widely studied as metamaterials [6], in acoustics as phononic crystals
 96 [35], and in biomechanics as bone substitutes [36,37]. In this paper, we will highlight a particular
 97 situation for which the solution predicted by classic continuum mechanics is wrong even for very
 98 long wavelengths. It is important to note that the sensitivity of the mechanical behavior to the lack of
 99 centrosymmetry can also manifest in statics [38–40].

100 The paper is organized as follows: in section 2 the gyroid lattice is described. In section 3 the
 101 Bloch-Floquet analysis is introduced along with some necessary definitions for polarization studies.
 102 Dispersion analysis is performed and discussed in section 4. Section 5 compares the results from
 103 section 4 to those obtained in the LW-LF approximation. Finally, some conclusions are drawn in
 104 section 6.

105 *Notations*

Throughout this paper, the Euclidean space \mathcal{E}^3 is equipped with a rectangular Cartesian coordinate system with origin O and an orthonormal basis $\mathcal{B} = \{\mathbf{e}_1, \mathbf{e}_2, \mathbf{e}_3\}$. Upon the choice of a reference point O in \mathcal{E}^3 , the Euclidean space and its underlying vector space E^3 can be considered as coincident. As a consequence, points will be designated by their vector positions with respect to O . For the sake of simplicity, E^3 will, from now on, simply be denoted E . In the following, \mathbf{r} will designate the position vector of a point P , and, with respect to \mathcal{B} ,

$$\mathbf{r} = x\mathbf{e}_1 + y\mathbf{e}_2 + z\mathbf{e}_3.$$

106 When needed, Einstein summation convention is used, i.e., when an index appears twice in an
 107 expression, it implies summation of that term over all the values of the index. The dot operator (\cdot)
 108 stands for the scalar product, the \wedge for the cross product and δ_{ij} is the Kronecker delta.
 109 Moreover, the following convention is retained:

- 110 • Blackboard fonts will denote tensor spaces: \mathbb{T} ;
- 111 • Tensors of order > 1 will be denoted using uppercase Roman Bold fonts: \mathbf{T} ;
- 112 • Vectors will be denoted by lowercase Roman Bold fonts: \mathbf{t} .

113 The orthogonal group in \mathbb{R}^3 is defined as $O(3) = \{\mathbf{Q} \in GL(3) | \mathbf{Q}^T = \mathbf{Q}^{-1}\}$, in which $GL(3)$ denotes
 114 the set of invertible transformations acting on \mathbb{R}^3 .

115 2. The gyroid lattice

116 The gyroid is a triply periodic minimal surface introduced for the first time in [41,42]. Since it is a
 117 minimal surface, it has a zero mean curvature, meaning that every point on the surface is a saddle
 118 point with equal and opposite principal curvatures [43]. It is periodic with respect to three orthogonal
 119 space vectors and is chiral, meaning that the surface only possesses rotation symmetry elements or,
 120 equivalently, that it does not possess any symmetry plane nor symmetry center [44].

121 2.1. Parametrization of the gyroid lattice

The gyroid's morphology is usually described using a level surface given by the following equation:

$$\phi(x, y, z; a, b) = 0 \quad (1)$$

with a and b real parameters and x, y, z coordinates of the position vector \mathbf{r} . In this paper, we will focus on a particular gyroid defined by :

$$\phi(x, y, z; a, b) := \sin 2\pi ax \cos 2\pi ay + \sin 2\pi ay \cos 2\pi az + \sin 2\pi az \cos 2\pi ax - b, \quad (2)$$

that exists only in the range $|b| < \sqrt{2}$ [44]. Indeed, beyond this peculiar value of b , it is possible to show that the surface described by ϕ presents discontinuities located at the borders of the fundamental (or asymmetrical) unit cell. A proof of this geometric constraint is provided in Appendix C. Due to its chiral nature, the gyroid surface exists in two enantiomorphic forms : dextrogyre and levogyre. The surface described by the implicit equation Equation 1 will be, arbitrarily, chosen to be the dextrogyre form. The levogyre form of the implicit equation is easily obtained by applying, for instance, the transformation $x \rightarrow -x$ in the Equation 1 . From the definition of the surface, one can then obtain a volume by defining the presence of matter for points satisfying the following inequality:

$$\phi(x, y, z; a, b) > 0. \quad (3)$$

122 The parameter a controls the spatial period while the parameter b controls the porosity . Examples of
 123 unit cells of such solids obtained with different values of b are plotted in Figure 1.

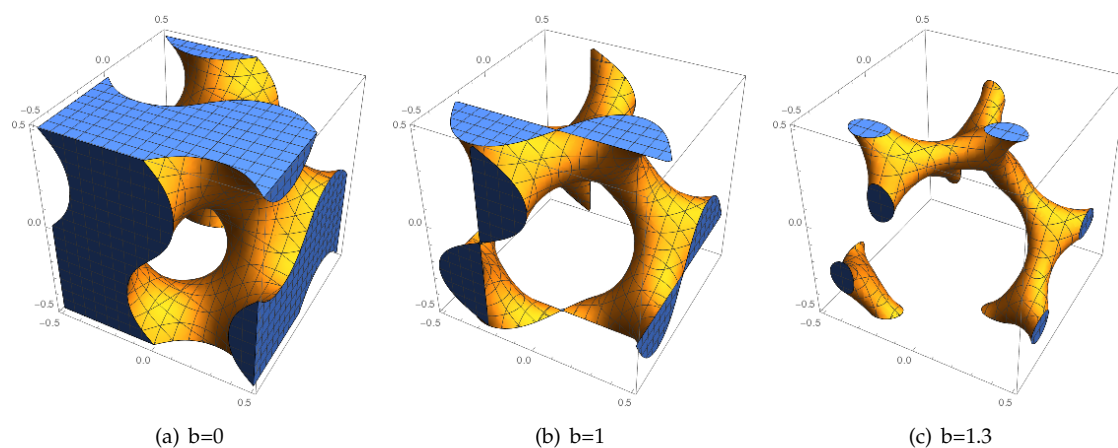


Figure 1. The unit cells of gyroid lattices obtained for different values of the parameter b . Despite what the angle of view may suggest, all these structures are simply connected.

The relationship between the porosity p and the parameter b is not analytical but can be estimated numerically. As can be observed in Figure 2 this relationship is almost linear and for porosities between 0.2 and 0.8, the following linearized formula can be used to estimate the porosity:

$$p = -0.325b + 0.5.$$

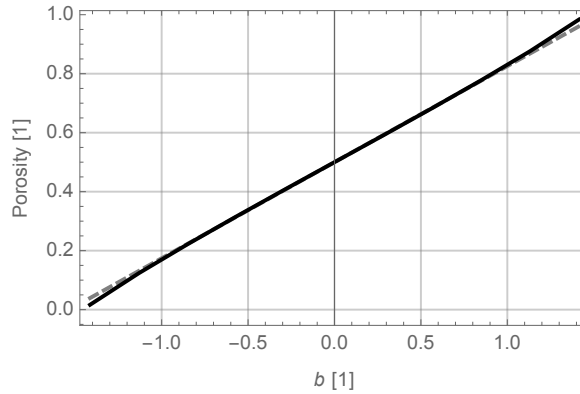


Figure 2. The relationship between the parameter b and the porosity, dashed line represents a linear approximation of real porosity plotted in plain line. The evaluation of the porosity is obtained numerically.

124

125 2.2. Symmetry properties

126 Thanks to its triply periodic nature, the gyroid structure can be considered as a crystal [35] with
 127 Body Centred Cubic (BCC) Bravais lattice and point group \mathcal{O} , using group theoretic notation [45], or
 128 432 using Hermann-Mauguin notation. It should be noted that this cubic group only contains rotations³,
 129 the geometry of the gyroid is hence chiral. The symmetry of the spatial structure is described by
 130 the space group, which details how transformations from the Bravais lattice and the point group are
 131 combined in the actual crystal. The space group (\mathcal{SG}) of the gyroid crystal is, using Hermann-Mauguin
 132 notation, $I4_132$ (space group #214 in the International Tables of Crystallography [46]), where the I
 133 stands for body-centered (BC), meaning that the conventional unit cell defined in crystallography is
 134 not primitive, but body-centered (more details provided in subsection 2.3). This space group contains
 135 screw axes and, as such, is not symmorphic⁴.

If \mathcal{C} stands for the "crystal" structure, and \star for the group action as defined in Appendix section B

$$\forall \mathbf{r} \in \mathcal{C}, \forall g \in \mathcal{SG}, \quad \mathbf{r}' = g \star \mathbf{r} \in \mathcal{C}.$$

From the generating transformations defined in Appendix B and using the equation of the gyroid surface (c.f. Equation 1) it is straightforward to verify that

$$\forall g \in \mathcal{SG}, \quad \phi(g \star \mathbf{r}) = \phi(\mathbf{r}).$$

136 2.3. Unit cell

Due to the periodicity of the geometry, the study of the gyroid structure can be restricted to a *unit cell*

$$\forall \mathbf{r} \in \mathbf{E}, \exists (\mathbf{r}_0, \mathbf{t}) \in (\mathcal{T}, \mathcal{R}), \quad \mathbf{r} = \mathbf{r}_0 + \mathbf{t} \quad (4)$$

³ To be more specific there are 3 different cubic point groups: \mathcal{O} , \mathcal{O}^- and $\mathcal{O} \oplus \mathbb{Z}_2^c$. The first one just contains rotations, the group is hence chiral and non-centrosymmetric. The second, \mathcal{O}^- , possesses symmetry planes but not the inversion, the group is achiral and non-centrosymmetric. The last group $\mathcal{O} \oplus \mathbb{Z}_2^c$ is centrosymmetric hence achiral. Some details are provided in the Appendix A, and more information can be found in [23].

⁴ A space group is called symmorphic if, apart from the lattice translations, all generating symmetry operations leave one common point fixed. Permitted as generators are thus only the point-group operations: rotations, reflections, inversions and rotoinversions. The symmorphic space groups may be easily identified because their Hermann-Mauguin symbol does not indicate a glide or screw operation.

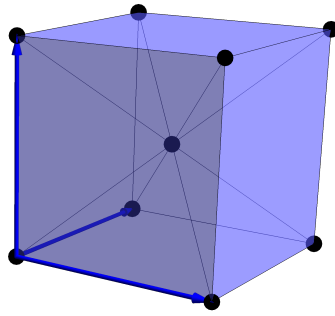


Figure 3. The conventional unit cell. The lattice vectors are indicated in blue.

where \mathcal{T} designates a unit cell and \mathcal{R} a periodicity lattice. It can be convenient to chose a reference unit cell from which other unit cells will be defined using lattice vectors \mathbf{a}_i and a triplet (n^1, n^2, n^3) combined as follow: $\mathbf{t} = n^1\mathbf{a}_1 + n^2\mathbf{a}_2 + n^3\mathbf{a}_3$, $n_i \in \mathbb{Z}$. The triplet $(0, 0, 0)$ is then associated to the reference unit cell. Once a lattice basis chosen, the considered unit cell is defined as follows,

$$\mathcal{T}_C = \{\mathbf{r}_0 \in E | \mathbf{r}_0 = r\mathbf{a}_1 + s\mathbf{a}_2 + t\mathbf{a}_3, (r, s, t) \in [0, 1]^3\}$$

and the associated periodicity lattice is given by:

$$\mathcal{R}_C = \{\mathbf{t} \in E | \mathbf{t} = n^1\mathbf{a}_1 + n^2\mathbf{a}_2 + n^3\mathbf{a}_3, n_i \in \mathbb{Z}\}$$

137 These geometrical sets can have been described using lattice vectors \mathbf{a}_i , gathered into a basis as
 138 $\mathcal{B}' = \{\mathbf{a}_1, \mathbf{a}_2, \mathbf{a}_3\}$. Note that they can as well be described with respect to the basis $\mathcal{B} = \{\mathbf{e}_1, \mathbf{e}_2, \mathbf{e}_3\}$ of E .

139

140 Among all the possible unit cells, some are special and have been given a standard name in the
 141 crystallography community: the *conventional unit cell* (CUC) and *primitive unit cell* (PUC).

142 The *conventional unit cell* (CUC) of the a BCC lattice is depicted in Figure 3. It is defined as the
 143 smallest cell having its edges along the symmetry directions of the Bravais lattice. Notice that, for
 144 body centered (BC) lattice, this unit cell is not minimal and a so-called *primitive unit cell* (PUC) can be
 145 considered instead. For a continuous structure tiling of the space, the primitive unit cell is defined as
 146 the smallest tile that generates the whole tiling using only translations. As such the primitive unit cell
 147 is a *fundamental domain* with respect to translational symmetries only.

148 2.3.1. BCC Conventional Unit Cell

149 For a BCC lattice, the conventional unit cell is defined as depicted in Figure 3. As its faces are
 150 perpendicular to Bravais lattice directions, despite its non minimality, this unit cell is easy to use
 151 for numerical computations. In this case, the conventional lattice vectors \mathbf{a}_i , are chosen such that
 152 $\mathbf{a}_i \wedge \mathbf{e}_i = \mathbf{0}$.

153 2.3.2. BCC Primitive Unit Cell

For a BCC lattice, two possible primitive unit cells (PUC) are represented in Figure 4. The primitive
 lattice vectors \mathbf{a}_i are not unique and the ones for the PUC depicted in Figure 4a) are defined as:

$$\mathbf{b}_1 = \frac{a}{2}(\mathbf{e}_1 + \mathbf{e}_2 - \mathbf{e}_3), \quad \mathbf{b}_2 = \frac{a}{2}(-\mathbf{e}_1 + \mathbf{e}_2 + \mathbf{e}_3), \quad \mathbf{b}_3 = \frac{a}{2}(\mathbf{e}_1 + \mathbf{e}_2 + \mathbf{e}_3),$$

while the ones presented in Figure 4b) are defined as:

$$\mathbf{b}'_1 = a\mathbf{e}_1, \quad \mathbf{b}'_2 = a\mathbf{e}_2, \quad \mathbf{b}'_3 = \frac{a}{2}(\mathbf{e}_1 + \mathbf{e}_2 + \mathbf{e}_3).$$

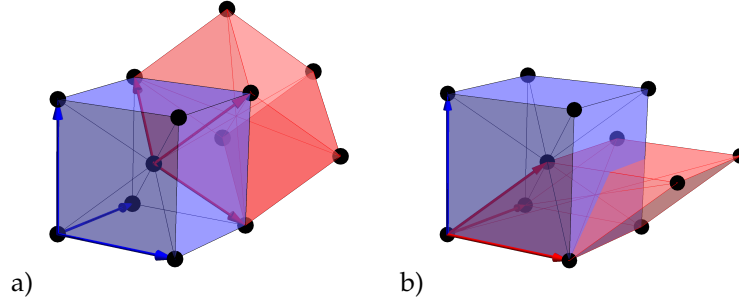


Figure 4. Two examples of primitive unit cells. The lattice vectors are indicated in red

They form $\mathcal{P} = \{\mathbf{b}_i\}_{1 \leq i \leq 3}$ and $\mathcal{P}' = \{\mathbf{b}'_i\}_{1 \leq i \leq 3}$ two other bases of E , which metric tensors are given by:

$$g(\mathcal{P}) = (\mathbf{b}_i \cdot \mathbf{b}_j) = \frac{a^2}{4} \begin{pmatrix} 3 & -1 & -1 \\ -1 & 3 & -1 \\ -1 & -1 & 3 \end{pmatrix}, \quad g(\mathcal{P}') = (\mathbf{b}'_i \cdot \mathbf{b}'_j) = \frac{a^2}{4} \begin{pmatrix} 4 & 0 & 2 \\ 0 & 4 & 2 \\ 2 & 2 & 3 \end{pmatrix}.$$

154 Being defined by a more symmetrical set of vectors \mathcal{P} , only the first primitive unit cell will be
155 considered here after.

156 2.4. Reciprocal basis and Brillouin Zone

The vector space dual to E is symbolized by E^* , and is formally defined as the space of linear forms on E ,

$$\forall l \in E^*, \forall \mathbf{u} \in E, l(\mathbf{u}) = \alpha \in \mathbb{R}.$$

Upon the choice of a scalar product the two spaces can be identified

$$(\forall l \in E^*, \exists \mathbf{v} \in E), \forall \mathbf{u} \in E, l(\mathbf{u}) = \mathbf{v} \cdot \mathbf{u} = \alpha \in \mathbb{R}$$

and from a basis of E a basis of E^* can be constructed. In the field of physics, E^* corresponds to the space of wavevectors, and a generic element of E^* is denoted by \mathbf{k} . For our applications, it is fundamental to introduce the reciprocal lattice \mathcal{R}^* of \mathcal{R} :

$$\mathcal{R}^* = \{\boldsymbol{\zeta} \in E^* | \boldsymbol{\zeta} = \zeta_1 \mathbf{a}^{*1} + \zeta_2 \mathbf{a}^{*2} + \zeta_3 \mathbf{a}^{*3}, \zeta_i \in \mathbb{Z}\}.$$

The vectors $(\mathbf{a}^{*1}, \mathbf{a}^{*2}, \mathbf{a}^{*3})$ constitute the lattice basis \mathcal{B}^* of \mathcal{R}^* and verify

$$\mathbf{a}^{*i} \cdot \mathbf{a}_j = \delta_{ij}, \quad \text{where} \quad \delta_{ij} = \begin{cases} 1 & \text{if } i = j, \\ 0 & \text{if } i \neq j. \end{cases} \quad (5)$$

\mathcal{B}^* can be computed from any lattice basis $(\mathbf{a}_1, \mathbf{a}_2, \mathbf{a}_3)$ of \mathcal{R} according to

$$\mathbf{a}^{*1} = \frac{\mathbf{a}_2 \wedge \mathbf{a}_3}{\mathbf{a}_1 \cdot (\mathbf{a}_2 \wedge \mathbf{a}_3)}, \quad \mathbf{a}^{*2} = \frac{\mathbf{a}_3 \wedge \mathbf{a}_1}{\mathbf{a}_2 \cdot (\mathbf{a}_3 \wedge \mathbf{a}_1)}, \quad \mathbf{a}^{*3} = \frac{\mathbf{a}_1 \wedge \mathbf{a}_2}{\mathbf{a}_3 \cdot (\mathbf{a}_1 \wedge \mathbf{a}_2)}. \quad (6)$$

Due to the following property,

$$\forall (\mathbf{t}, \boldsymbol{\zeta}) \in \mathcal{R} \times \mathcal{R}^*, \quad e^{2\pi i \boldsymbol{\zeta} \cdot \mathbf{t}} = 1 \quad (7)$$

vectors of the reciprocal lattice are the supports of \mathcal{R} -periodic functions on E since,

$$\forall (\mathbf{r}_0, \mathbf{t}) \in \mathcal{T} \times \mathcal{R}, \quad f(\mathbf{r}_0 + \mathbf{t}) = \sum_{\boldsymbol{\zeta} \in \mathcal{R}^*} \lambda_{\boldsymbol{\zeta}} e^{2\pi i \boldsymbol{\zeta} \cdot (\mathbf{r}_0 + \mathbf{t})} = \sum_{\boldsymbol{\zeta} \in \mathcal{R}^*} \lambda_{\boldsymbol{\zeta}} e^{2\pi i \boldsymbol{\zeta} \cdot \mathbf{r}_0} e^{2\pi i \boldsymbol{\zeta} \cdot \mathbf{t}} = f(\mathbf{r}_0).$$

In addition, use will be made of the *First Brillouin Zone* (FBZ) \mathcal{T}^* of the reciprocal lattice \mathcal{R}^* defined as:

$$\mathcal{T}^* := \{\mathbf{k} \in \mathbb{E}^* | \forall \boldsymbol{\zeta} \in \mathcal{R}^* - 0, \|\mathbf{k}\| < \|\mathbf{k} - \boldsymbol{\zeta}\|\} \quad (8)$$

Using the reciprocal lattice \mathcal{R}^* and the FBZ \mathcal{T}^* , any wavevector \mathbf{k} can be expressed as

$$\forall \mathbf{k} \in \mathbb{E}^*, \exists (\mathbf{k}_0, \boldsymbol{\zeta}) \in (\mathcal{T}^*, \mathcal{R}^*), \quad \mathbf{k} = \mathbf{k}_0 + \boldsymbol{\zeta}.$$

157 We can geometrically interpret \mathcal{T}^* as the set of wavevectors \mathbf{k} which are closer to the null
 158 wavevector than to any other wavevector $\boldsymbol{\zeta}$ of the reciprocal lattice \mathcal{R}^* . It is the *Wigner-Seitz* cell of the
 159 reciprocal lattice, this cell is uniquely defined and independent of the choice of \mathcal{T} . Similarly to the
 160 primitive unit cell in the direct space, the FBZ is a fundamental domain with respect to translations.
 161 Physically, the wavelength λ is defined as the inverse of the wavenumber, which is the norm of the
 162 wavevector : $\lambda = 1/\|\mathbf{k}\|$. Then, wavevectors belonging to \mathcal{T}^* have wavelengths that are greater
 163 than the wavelength of the periodicity lattice. When $\|\mathbf{k}\| \rightarrow 0$ the wavelength becomes infinite,
 164 sollicitations varying with almost null wavenumber are said to be *scale separated* with respect to the
 165 periodicity lattice. This is usually the regime in which the LW approximation of elastodynamics
 166 homogenization holds.

167 The FBZ can be further reduced if we consider also the symmetry operations of the point group. The
 168 result is an *Irreducible Brillouin Zone* (IBZ), that is delimited by points of high symmetry, summarized
 169 for the considered gyroid lattice in [Table 1](#). In this table, the high symmetry points are given in
 170 the non-orthogonal reciprocal lattice basis \mathcal{P}^* , dual to the primitive lattice basis \mathcal{P} as well as in the
 171 orthonormal lattice basis \mathcal{B} which coincides with its dual in the reciprocal space. The path obtained
 172 connecting these high symmetry points along the edges of the IBZ is often used to characterize the
 173 photonic and phononic properties of the lattice [6,26]. However, it has been pointed out that this
 174 choice is not always reliable as some relevant information, e.g. about band gaps, could be missing [47].

175

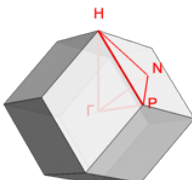
In this paper we consider the basis \mathcal{P} , that corresponds to the one depicted in [Figure 4a](#)). The reciprocal lattice is itself a Bravais lattice, and in the case of BCC lattice, it is a Face Centered Cubic (FCC) lattice. Using [Equation 6](#), the reciprocal basis \mathcal{P}^* is equal to

$$\mathbf{a}^{*1} = \frac{1}{a}(\mathbf{e}_1 + \mathbf{e}_2), \quad \mathbf{a}^{*2} = \frac{1}{a}(\mathbf{e}_2 + \mathbf{e}_3), \quad \mathbf{a}^{*3} = \frac{1}{a}(\mathbf{e}_1 + \mathbf{e}_3).$$

The metric tensor of \mathcal{P}^* is the inverse of the one of \mathcal{P}

$$g(\mathcal{P}^*) = g(\mathcal{P})^{-1} = \frac{1}{a^2} \begin{pmatrix} 2 & 1 & 1 \\ 1 & 2 & 1 \\ 1 & 1 & 2 \end{pmatrix}$$

Table 1. The high symmetry points of the gyroid lattice. The group notations are detailed in [Appendix section A](#).

Symmetry point	Coordinates w.r.t. \mathcal{P}^* (k_1, k_2, k_3)	Coordinates w.r.t. \mathcal{B} (x_1, x_2, x_3)	Point Group (Math.)	Point Group (H-M)	Illustration of the first Brillouin zone
Γ	(0, 0, 0)	(0, 0, 0)	\mathcal{O}	432	
H	$(-\frac{1}{2}, \frac{1}{2}, \frac{1}{2})$	$(0, 0, \frac{1}{a})$	\mathcal{O}	432	
P	$(\frac{1}{4}, \frac{1}{4}, \frac{1}{4})$	$(\frac{1}{2a}, \frac{1}{2a}, \frac{1}{2a})$	D_3	32	
N	$(0, \frac{1}{2}, 0)$	$(0, \frac{1}{2a}, \frac{1}{2a})$	D_2	222	

176 3. Analysis tools

177 In the previous section we characterized the lattice from the point of view of crystallography. In
 178 this next section we will use these results to compute the elastodynamic response of the lattice. The
 179 objective of the present section is to provide the analysis tools to be used to perform the computation
 180 and to interpret the results.

181 3.1. Bloch-Floquet analysis

Since the material is periodic, the dispersion diagram will be computed using Bloch-Floquet analysis [48]. The elastodynamics equation for the periodic continuum reads

$$\operatorname{div} [\mathbb{C}(\mathbf{r}) : (\mathbf{u}(\mathbf{r}) \otimes \nabla)] = \rho(\mathbf{r})\ddot{\mathbf{u}}(\mathbf{r}) \quad (9)$$

where $\rho(\mathbf{r})$ is the \mathcal{R} -periodic mass density and $\mathbb{C}(\mathbf{r})$ is the \mathcal{R} -periodic fourth-order elasticity tensor. As we saw in subsection 2.3, each cell of the assembly can be identified by the triplet (n^1, n^2, n^3) , where the triplet $(0, 0, 0)$ is conventionally assigned to the reference unit cell. The position of a point \mathbf{r} of the (n^1, n^2, n^3) -cell is obtained from the position of a point in the reference unit cell \mathbf{r}_0 by Equation 4 where $\mathbf{t} = n^p \mathbf{a}_p$. Being \mathcal{R} -periodic, $\rho(\mathbf{r})$ and $\mathbb{C}(\mathbf{r})$ verify:

$$\forall (\mathbf{r}_0, \mathbf{t}) \in \mathcal{T} \times \mathcal{R}, \rho(\mathbf{r}_0 + \mathbf{t}) = \rho(\mathbf{r}_0), \mathbb{C}(\mathbf{r}_0 + \mathbf{t}) = \mathbb{C}(\mathbf{r}_0)$$

Thanks to the Floquet-Bloch theorem [48], elementary solutions to the Equation 9 over \mathcal{C} can be searched for in the form of Bloch-waves :

$$\mathbf{u}_{\mathbf{k}}(\mathbf{r}_0) = \mathbf{U}_{\mathbf{k}}(\mathbf{r}_0) e^{2\pi i(f t - \mathbf{k} \cdot \mathbf{r}_0)}, \quad \mathbf{U}_{\mathbf{k}} \in \mathbb{C}^3, \quad (10)$$

182 where $\mathbf{U}_{\mathbf{k}}$ is the complex polarisation vector which is \mathcal{R} -periodic in space and constant in time, f is
 183 the frequency of the Bloch-wave and \mathbf{k} its wavevector⁵. $\mathbf{U}_{\mathbf{k}}$ describes the movement of matter as the
 184 wave propagates. In the case of an homogeneous material the polarization vector becomes constant in
 185 space and the classical plane wave solution is retrieved. Since the displacement field in Equation 10 is
 186 complex valued, its real part should be computed in order to retrieve the physical solution.

From its definition as a Bloch-wave, the displacement at a point \mathbf{r} image of the $\mathbf{r}_0 \in \mathcal{T}$ by a translation $\mathbf{t} \in \mathcal{R}$ has the following expression

$$\mathbf{u}_{\mathbf{k}}(\mathbf{r}) = \mathbf{u}_{\mathbf{k}}(\mathbf{r}_0 + \mathbf{t}) = \mathbf{U}_{\mathbf{k}}(\mathbf{r}_0 + \mathbf{t}) e^{2\pi i(f t - \mathbf{k} \cdot (\mathbf{r}_0 + \mathbf{t}))} = \mathbf{u}_{\mathbf{k}}(\mathbf{r}_0) e^{-2\pi i \mathbf{k} \cdot \mathbf{t}} \quad (11)$$

187 The physical meaning is that the displacement vector at two homologous points⁶ only differs by a
 188 phase factor.

Additionally, the Bloch-wave expression in Equation 10 has the interesting property to be also \mathcal{R}^* -periodic. Indeed, due to its \mathcal{R} -periodicity, $\mathbf{U}_{\mathbf{k}}(\mathbf{r}_0)$ can be decomposed as a Fourier series, leading to the equivalent expression for $\mathbf{u}_{\mathbf{k}}(\mathbf{r}_0)$:

$$\mathbf{u}_{\mathbf{k}}(\mathbf{r}_0) = \sum_{\xi \in \mathcal{R}^*} \tilde{\mathbf{U}}_{\mathbf{k} + \xi} e^{2\pi i(f t - (\mathbf{k} + \xi) \cdot \mathbf{r}_0)}$$

189 where $\tilde{\mathbf{U}}_{\mathbf{k} + \xi}$ stands for the Fourier coefficients of the series expansion. Using this particular form, the
 190 \mathcal{R}^* -periodicity of the Bloch-waves is easily proven using the change of variable $\tilde{\xi} = \xi + \xi^*$:

⁵ It is important to remark that wavevectors \mathbf{k} follow the so-called "crystallographer's definition" which consists in dropping the often seen 2π coefficient. This implies, for instance, that the norm $\|\mathbf{k}\|$, i.e. the wavenumber, is directly the inverse of the wavelength λ , which is more convenient for physical interpretation of results.

⁶ Two points $\mathbf{r}_1, \mathbf{r}_2$ and are said homologous if $\mathbf{r}_1 - \mathbf{r}_2 \in \mathcal{R}$.

$$\mathbf{u}_{\mathbf{k}+\tilde{\zeta}^*}(\mathbf{r}_0) = \sum_{\tilde{\zeta} \in \mathcal{R}^*} \tilde{\mathbf{U}}_{\mathbf{k}+\tilde{\zeta}^*+\tilde{\zeta}} e^{2\pi i(ft - (\mathbf{k}+\tilde{\zeta}^*+\tilde{\zeta}) \cdot \mathbf{r}_0)} = \sum_{\tilde{\zeta} \in \mathcal{R}^*} \tilde{\mathbf{U}}_{\mathbf{k}+\tilde{\zeta}} e^{2\pi i(ft - (\mathbf{k}+\tilde{\zeta}) \cdot \mathbf{r}_0)} = \mathbf{u}_{\mathbf{k}}(\mathbf{r}_0)$$

191 The main consequence of this property is that the characterization of the elastodynamics behavior of a
 192 periodic material does not require to investigate the mechanical response to all the $\mathbf{k} \in E^*$ but can be
 193 restricted to the study of $\mathbf{k} \in \mathcal{T}^*$ via \mathcal{R}^* -periodicity of the wavevector, where \mathcal{T}^* corresponds to the
 194 First Brillouin Zone (FBZ), as introduced in 2.3.

195 3.2. Polarization of waves in homogeneous materials

Before presenting the results, it is useful to recall some definitions concerning the polarization of elastic waves in homogeneous materials. Let's take us back to the Bloch-wave ansatz introduced in Equation 10, since the material is now considered homogeneous, the polarization vector $\mathbf{U}_{\mathbf{k}}$ is constant both in space and time. In the most general case, the complex polarization vector $\mathbf{U}_{\mathbf{k}}$, that will be denoted \mathbf{U} from now on for the sake of simplicity, can be decomposed in its real and imaginary parts as follows:

$$\mathbf{U} = \mathbf{U}^{\mathbb{R}} + i\mathbf{U}^{\mathbb{C}}.$$

An interpretation of this decomposition, and of its consequences on wave propagation, can be obtained by considering the real part of Equation 10 :

$$\hat{\mathbf{u}} = \text{Re}(\mathbf{u}) = \mathbf{U}^{\mathbb{R}} \cos(2\pi(ft - \mathbf{k} \cdot \mathbf{r})) - \mathbf{U}^{\mathbb{C}} \sin(2\pi(ft - \mathbf{k} \cdot \mathbf{r})).$$

196 Since the vectors $\mathbf{U}^{\mathbb{R}}$ and $\mathbf{U}^{\mathbb{C}}$ are independent, the polarization of the displacement can be very
 197 rich. Its precise nature is directly related to conditions on $\mathbf{U}^{\mathbb{R}}$ and $\mathbf{U}^{\mathbb{C}}$, as summarized in Table 2.
 198 It is important to remark that different conventions are used to define the handedness of circularly
 199 polarized waves. In this paper, we will consider that a wave is right handed if it follows the curl of the
 200 fingers of a right hand whose thumb is directed towards the wave propagation, away from the source.
 201 In the table, the unit normal vector defining the direction of propagation is defined by $\mathbf{n} = \frac{\mathbf{k}}{\|\mathbf{k}\|}$.

Table 2. The polarizations of plane waves and conditions on the complex amplitude.

polarization	Condition
Transverse polarization	$\mathbf{U} \wedge \mathbf{n} = \mathbf{0}$
Longitudinal polarization	$\mathbf{U} \cdot \mathbf{n} = 1$
Linear polarization	$\mathbf{U}^{\mathbb{R}} \wedge \mathbf{U}^{\mathbb{C}} = \mathbf{0}$
Elliptic polarization	$\mathbf{U}^{\mathbb{R}} \wedge \mathbf{U}^{\mathbb{C}} \neq \mathbf{0}$
Circular polarization	$\mathbf{U} \cdot \mathbf{U} = 0$
↳ Right handedness	$\mathbf{n} \cdot (\mathbf{U}^{\mathbb{R}} \wedge \mathbf{U}^{\mathbb{C}}) < 0$
↳ Left handedness	$\mathbf{n} \cdot (\mathbf{U}^{\mathbb{R}} \wedge \mathbf{U}^{\mathbb{C}}) > 0$

202 Thus, a complex polarization vector can lead to a phase shift between the components of the
 203 displacement vector $\hat{\mathbf{u}}$, and thus to a polarization that is other than linear, see Figure 5 for illustration
 204 of a linear and two circular polarizations with opposite handedness.

205 4. Dispersion analysis using Finite Elements Analysis (FEA)

206 In order to investigate the ultrasonic properties of the gyroid lattice, and given the periodicity of
 207 the architecture as described in the previous sections, an approach based on Bloch-Floquet analysis
 208 will be followed. For the sake of simplicity, the conventional unit cell depicted in Figure 6 is used
 209 to define the numerical model. For the investigation of the elastodynamic properties of the gyroid
 210 crystal, the wavevector will be restricted to the boundaries of the Irreducible Brillouin Zone (IBZ),
 211 as depicted in red in Figure 7a. The high symmetry points of this IBZ are defined in Table 1. The

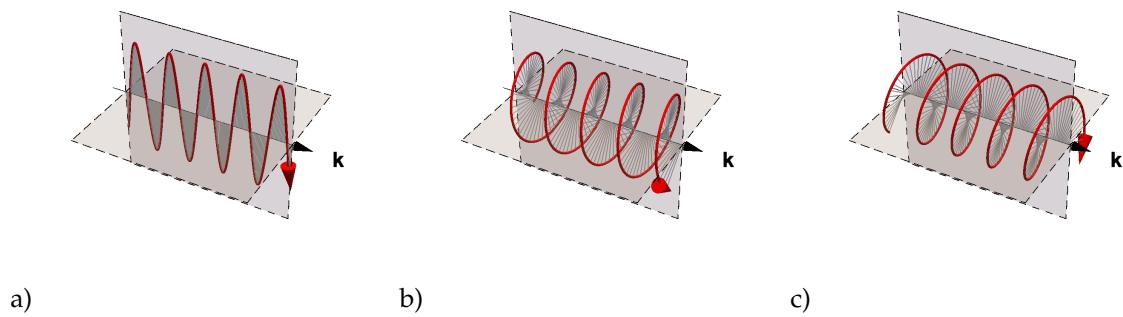


Figure 5. Some examples of polarizations: a) linear, b) Circular right handed, c) Circular left handed.

212 model has been implemented using the commercial software Comsol Multiphysics and considering
 213 titanium as constitutive material, the parameters of which are displayed in [Table 3](#). The mesh of the
 214 unit cell is presented in [Figure 6](#), and it consists of 66,232 tetrahedral elements. Lagrange quadratic
 215 elements are used, for a total of 329,277 degrees of freedom. Periodic Bloch-Floquet conditions are
 216 implemented by imposing them as displacement conditions at the boundaries, following [Equation 11](#).
 217 Then, the wavenumber in \mathbf{k} is imposed and the corresponding frequencies are retrieved by solving the
 218 corresponding eigenvalue problem. The computation of each wavenumber took an average of 109
 219 seconds on a workstation equipped with an Intel(R) Xeon(R) CPU E5-1650 v2 at 3.50 GHz using six
 220 cores.

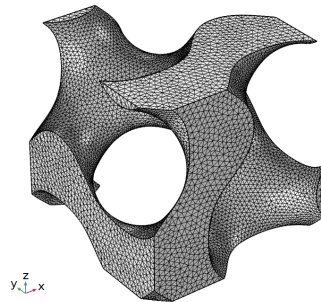


Figure 6. The meshed unit cell used in simulations

Table 3. The parameters used in the numerical simulations, corresponding to bulk titanium.

Mass Density [kg/m^2]	Young Modulus [GPa]	Poisson Ratio [1]	Porosity [1]	Unit cell size [mm]
ρ_b	E_b	ν_b	p	a
4506	115.7	0.321	0.7	1

221 The results of the dispersion analysis are depicted in [Figure 7\(a\)](#). It can be observed, qualitatively,
 222 that these results are similar to those obtained for electromagnetic waves in [6] (see [Figure 8](#)). In
 223 particular, the behavior of the acoustic branches, i.e. those branches starting from the origin Γ ,
 224 corresponding to transverse waves (gray lines in [Figure 7\(a\)](#)) is remarkably similar.

225 Since the objective of the paper is to investigate the behavior of the lattice within the LW-LF
 226 approximation given by classic continuum mechanics, the phase velocities and polarization of waves
 227 have been computed for large values of the wavelength with respect to the size of the unit cell – in
 228 this case $\|\mathbf{k}\| = 37 \text{ m}^{-1}$, that corresponds to a wavelength close to 26 times the size of the unit cell.
 229 For each mode, the polarization vector has been estimated by computing the average of the complex
 230 displacement of the eigen-mode over the unit cell, and the results are listed in [Table 4](#). We will now
 231 analyze the results along the following directions of propagation, also depicted in [Figure 7\(b\)](#):

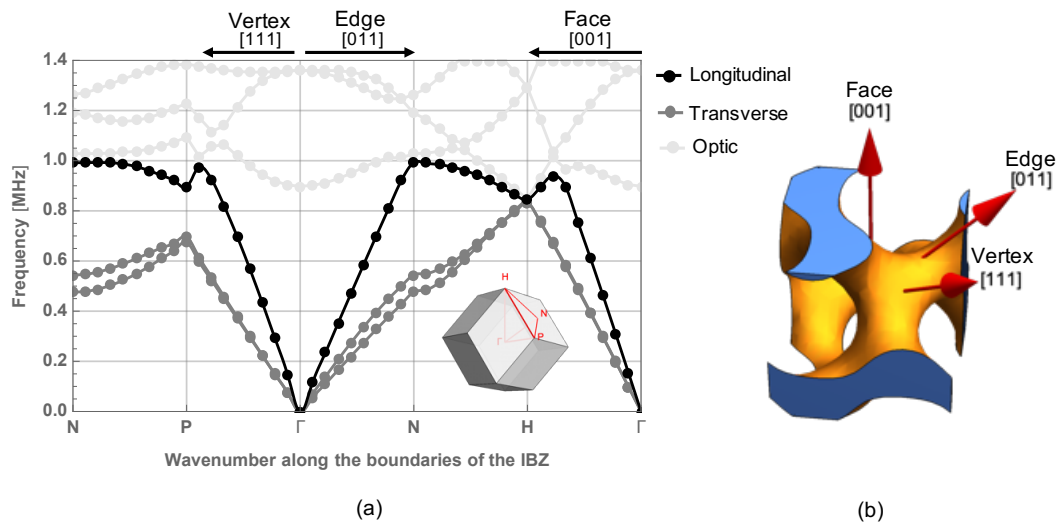


Figure 7. The dispersion diagram of the Gyroid lattice computed along the boundaries of the Irreducible Brillouin Zone (IBZ) and directions of propagation with respect to the unit cell. (a) The dispersion relation of the Gyroid lattice computed along the boundaries of the Irreducible Brillouin Zone (IBZ). (b) The direction of propagation with respect to the unit cell.”

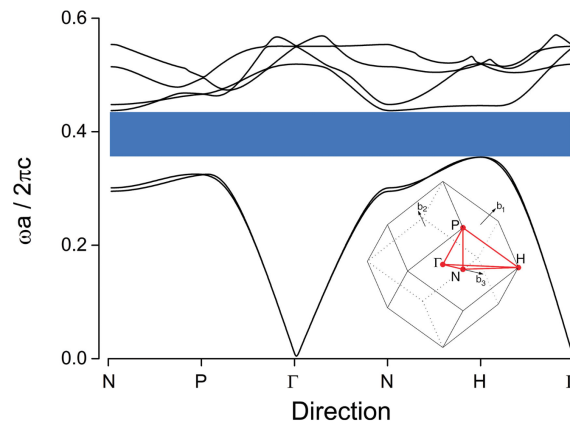


Figure 8. The photonic band diagram of a single gyroid photonic crystal. Reproduced with permission from [6].

- 232 • [001] : this direction is going from the center of the fundamental cell to the middle of a face. It
 233 corresponds to an axis of rotation of order 4 (rotations of $\pi/2$ rad);
 234 • [011] : this direction is going from the center of the fundamental cell to the middle of an edge. It
 235 corresponds to an axis of rotation of order 2 (rotations of π rad);
 236 • [111] : this direction is going from the center of the fundamental cell to a vertex. It corresponds
 237 to an axis of rotation of order 3 (rotations of $2\pi/3$ rad).

238 Using the conditions listed in Table 2, we have characterized the polarization for each of the above
 239 propagation directions. The results are summarized in Table 4.

240 Along the direction [001] a longitudinal wave propagating at 3018 m/s can be observed. The
 241 two transverse waves have eigenmodes with complex amplitude and propagate with the same phase
 242 velocity of 1932 m/s. These complex amplitudes correspond to two circularly polarized transverse
 243 waves, with opposite handedness. In the direction [011], a longitudinal wave propagating at 4595 m/s
 244 can be observed. One transverse wave is linearly polarized in direction [100], and propagates with
 245 a phase velocity of 2728 m/s. The last solution corresponds again to a transverse wave, linearly
 246 polarized along $(0, 1, -1)$, with velocity 2136 m/s. Finally, direction [111] has a linearly polarized

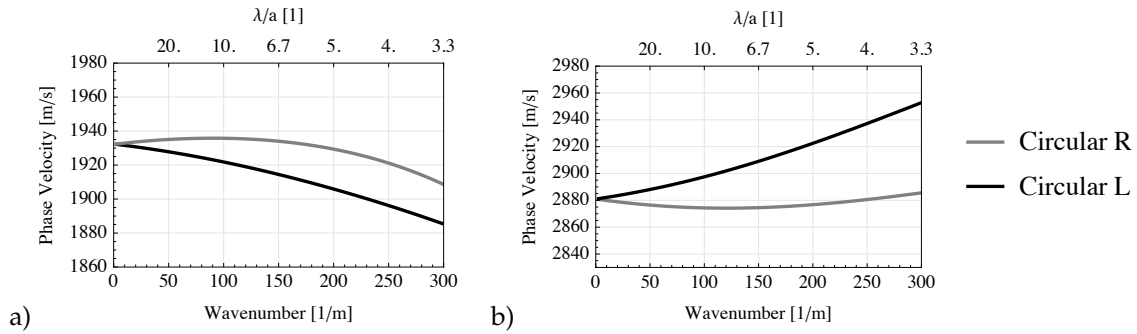


Figure 9.

247 longitudinal wave at 5757 m/s, and two circularly polarized waves with opposite handedness and
 248 propagating at the same velocity 2881 m/s.

249 In summary, circularly polarized waves exist only if the direction of propagation is along a
 rotation axis of symmetry of order greater than 2.

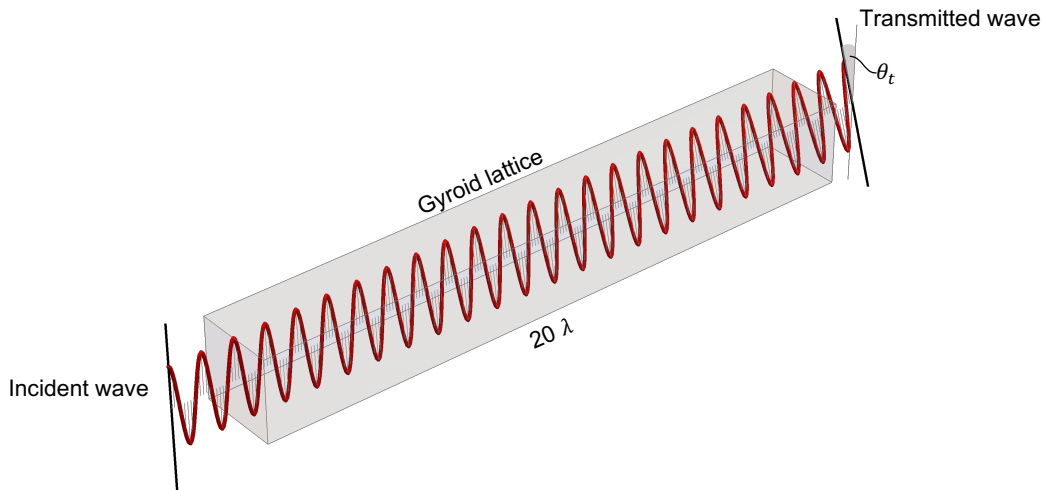


Figure 10.

250 Furthermore, the overall dispersion is *normal* for direction [001], i.e. phase velocity decreases
 251 when increasing the frequency, and *anomalous* for direction [001] (see [49] for the definition).
 252

Table 4. The phase velocity and polarization in the very long wavelength approximation.

Direction	Phase velocity [m/s]	Polarization (x_1, x_2, x_3)	Type of wave
[001]	3018	$(0, 0, 1)$	Longitudinal
	1932	$(i, 1, 0)$	Circular R \odot
	1932	$(1, -i, 0)$	Circular L \odot
[011]	4595	$(0, 1, 1)$	Longitudinal
	2728	$(1, 0, 0)$	Transverse
	2136	$(0, 1, -1)$	Transverse
[111]	5757	$(1, 1, 1)$	Longitudinal
	2881	$(-1 + i0.58, 1 + i0.55, -i1.13)$	Circular R \odot
	2881	$(-1 - i1.68, -1 + i1.72, 2 - i0.03)$	Circular L \odot

253 5. Long-Wavelength and Low-Frequency approximation and classic elasticity

In this last section we will introduce and identify the equivalent homogenized model in the framework of classic linear elasticity. This equivalent homogenized model is characterized by a couple of effective tensors ρ^H and C^H in such a way that the displacement field \mathbf{v} is solution of the following problem:

$$\operatorname{div} \left[C^H : (\mathbf{v}(\mathbf{r}) \otimes \nabla) \right] = \rho^H \ddot{\mathbf{v}}(\mathbf{r}) \quad (12)$$

254 where \mathbf{v} verifies $\langle \mathbf{u} \rangle = \mathbf{v}$, $\langle \cdot \rangle$ denotes the spatial average operator over \mathcal{T} and \mathbf{u} is the displacement
255 field solution to the heterogeneous problem Equation 9, as done for instance in [10].

Since the effective continuum is homogeneous, we consider a plane wave solution with $\mathbf{k} = f/c \mathbf{n}$ where c is the phase velocity of the wave and \mathbf{n} a unitary vector. The substitution of this wave solution and of a linear elastic constitutive law into Equation 12 leads to following equation

$$\Gamma \cdot \mathbf{U} = \rho c^2 \mathbf{U} \quad (13)$$

256 where $\Gamma = \mathbf{n} \cdot C^H \cdot \mathbf{n}$ is the Christoffel, or acoustic, tensor. The solution of the eigenvalue problem
257 stated in Equation 13 for a given direction \mathbf{n} gives the phase velocities and polarizations of waves in
258 the effective continuum.

In classical elasticity, a material with cubic symmetry is defined by three independent material constants. Using Mandel notation [53], the corresponding elastic tensor for a material having its symmetry axis parallel to is \mathcal{B} reads:

$$[\tilde{C}^H] = \begin{bmatrix} c_{11} & c_{12} & c_{12} & 0 & 0 & 0 \\ c_{12} & c_{11} & c_{12} & 0 & 0 & 0 \\ c_{12} & c_{12} & c_{11} & 0 & 0 & 0 \\ 0 & 0 & 0 & c_{44} & 0 & 0 \\ 0 & 0 & 0 & 0 & c_{44} & 0 \\ 0 & 0 & 0 & 0 & 0 & c_{44} \end{bmatrix}_{\mathcal{B}}$$

259 It is worth noting that classical elasticity is insensitive to the lack of centrosymmetry [54]. The symmetry
260 class of the elasticity tensor in the cubic system is $\mathcal{O} \oplus \mathbb{Z}_2^c$ meaning that even if the material symmetry
261 group of the unit cell does not contain the inversion, the symmetry group of elasticity tensor will
262 inherit it.

263 In the case of cubic materials, the solutions of Equation 13 listed in Table 5 are directly obtained. Using the phase velocities computed from the Floquet-Bloch analysis, parameters c_{11} , c_{12} , c_{44} and ρ_s

Table 5. The phase velocity and polarization in classic elasticity.

Direction	Phase velocities [m/s]	Polarization	Type of wave
[001]	$\sqrt{\frac{c_{11}}{\rho}} \approx 3018$	(0, 0, 1)	Longitudinal
	$\sqrt{\frac{c_{44}}{\rho}} \approx 1932$	(0, 1, 0)	Transverse
	$\sqrt{\frac{c_{44}}{\rho}} \approx 1932$	(1, 0, 0)	Transverse
[011]	$\sqrt{\frac{c_{11}+c_{12}+2c_{44}}{\rho}} \approx 4595$	(0, 1, 1)	Longitudinal
	$\sqrt{\frac{2c_{44}}{\rho}} \approx 2728$	(1, 0, 0)	Transverse
	$\sqrt{\frac{c_{11}-c_{12}}{\rho}} \approx 2136$	(0, 1, -1)	Transverse
[111]	$\sqrt{\frac{c_{11}+2c_{12}+4c_{44}}{\rho}} \approx 5757$	(1, 1, 1)	Longitudinal
	$\sqrt{\frac{c_{11}-c_{12}+c_{44}}{\rho}} \approx 2881$	(-1, 1, 0)	Transverse
	$\sqrt{\frac{c_{11}-c_{12}+c_{44}}{\rho}} \approx 2881$	(-1, -1, 2)	Transverse

Table 6. The material properties in the very long wavelength approximation.

Elastic coefficients			Mass density
c_{11} [GPa]	c_{12} [GPa]	c_{44} [GPa]	ρ [kg/m ³]
12.32	6.126	5.040	1351.8

264 can be identified and the homogeneous equivalent properties listed in Table 6 are then deduced. It
 265 can be noticed that, as presented in Table 5, since we considered the propagation along the rotational
 266 axes of symmetry, for each direction we observe a purely longitudinal wave and two purely transverse
 267 waves.

268 We now move on to comparing phase velocities and polarizations obtained from the Floquet-Bloch
 269 analysis with the ones forecast by the Long-Wavelength and Low-Frequency approximation using
 270 classical elasticity. We start with direction [001]. As already mentioned, this direction corresponds to a
 271 rotational axis of symmetry of order 4. In this case, as the elasticity tensor is non sensitive to chirality,
 272 the symmetry group of the physical phenomenon⁷ is conjugate to $D_4 \oplus Z_2^c$. Indeed, as the acoustic
 273 tensor defined in Equation 13 is a second-order tensor, the Hermann theorem of Crystal physics [11]
 274 predicts its behavior as transversely isotropic, i.e. $O(2) \oplus Z_2^c$. As a consequence Γ must have an
 275 eigenspace of dimension 2. . Moving to the results presented in Table 5, we can see that the classic
 276 theory indeed predicts one faster longitudinal wave and two slower transverse waves propagating
 277 with the same phase velocity.

278 Similar results are obtained for propagation along [111], which corresponds to rotational axis of
 279 symmetry of order 3. In this case the symmetry group of the physical phenomenon is conjugate to
 280 $D_3 \oplus Z_2^c$, and thus again transverse isotropy is imposed to the acoustic tensor. Finally, the direction
 281 of propagation [011] is along to a rotation axis of symmetry of order 2, the physical point group is
 282 thus conjugate to $D_2 \oplus Z_2^c$. Here, the symmetry class of the acoustic tensor is $D_2 \oplus Z_2^c$, and all the
 283 eigenspaces are unidimensional. In this last case, as this kind of symmetry can be seen by second order
 284 tensors, the results from FEA on the heterogeneous material and classic elasticity are in agreement in
 285 the LF-LW regime.

286 In this section we have shown that some discrepancies can be observed when using an overall
 287 homogeneous continuum of Cauchy type. Classical elasticity (as opposed to generalized elasticity)
 288 is not rich enough to capture certain specific physical phenomena related to the symmetries of the
 289 material. In particular, if phase velocities are correctly estimated the polarizations are incorrectly
 290 predicted. Moreover, as it is well known, the onset of dispersion when frequency or wavenumber
 291 increase cannot be described in the classic Cauchy model.

292 6. Conclusions

293 In this work we have shown that a classical continuum model cannot capture the correct behavior
 294 of elastic waves propagating in gyroid lattices. This is due to the fact that the classic continuum
 295 mechanics is insensitive to the lack of centrosymmetry of the architected material. However, it is
 296 a well established belief that the effects of noncentrosymmetry are only related to waves having a
 297 wavelength which compares to the size of the microstructure. Here we demonstrate that the solution
 298 given by the classical theory fails to predict the correct response, even in the Long Wavelength - Low
 299 Frequency domain.

300 In order to capture the onset of this unconventional behavior, called acoustical activity, the elastic
 301 continuum model needs to be enriched. Different strategies of enrichment are possible. In particular,
 302 the use of strain-gradient elasticity will be investigate in a forthcoming study.

⁷ The symmetry group of the physical phenomenon is the intersection of the symmetry group of the constitutive equations and the symmetry group of the mechanical solicitation.

303 **Author Contributions:**

304 **Funding:** The authors acknowledge the support of the French Agence Nationale de la Recherche (ANR), under
 305 grant ANR-19-CE08-0005 (project MaxOasis). This work was partially funded by CNRS/IRP Coss&Vita between
 306 Fédération Francilienne de Mécanique (F2M, CNRS FR2609) and M&MoCS

307 **Acknowledgments:**308 **Abbreviations**

309 The following abbreviations are used in this manuscript:

310

BCC	Body Centered Cubic
BZ	Brillouin Zone
IBZ	Irreducible Brillouin Zone
311 FEA	Finite Elements Analysis
FCC	Face Centered Cubic
LF	Low Frequency
LW	Long Wavelength

312 **Appendix A Dictionary**

313 To obtain the normal forms for the different classes the generators provided in the following table
 314 have been used :

Group	Generators
Z_2^-	$\mathbf{P}_{\mathbf{e}_3}$
Z_n	$\mathbf{R}\left(\mathbf{e}_3; \frac{2\pi}{n}\right)$
D_n	$\mathbf{R}\left(\mathbf{e}_3; \frac{2\pi}{n}\right), \mathbf{R}(\mathbf{e}_1; \pi)$
$Z_{2n}^-, n \geq 2$	$-\mathbf{R}\left(\mathbf{e}_3; \frac{\pi}{n}\right)$
$D_{2n}^h, n \geq 2$	$-\mathbf{R}\left(\mathbf{e}_3; \frac{\pi}{n}\right), \mathbf{R}(\mathbf{e}_1, \pi)$
D_n^v	$\mathbf{R}\left(\mathbf{e}_3; \frac{2\pi}{n}\right), \mathbf{P}_{\mathbf{e}_1}$
\mathcal{T}	$\mathbf{R}(\mathbf{e}_3; \pi), \mathbf{R}(\mathbf{e}_1; \pi), \mathbf{R}(\mathbf{e}_1 + \mathbf{e}_2 + \mathbf{e}_3; \frac{2\pi}{3})$
\mathcal{O}	$\mathbf{R}(\mathbf{e}_3; \frac{\pi}{2}), \mathbf{R}(\mathbf{e}_1; \pi), \mathbf{R}(\mathbf{e}_1 + \mathbf{e}_2 + \mathbf{e}_3; \frac{2\pi}{3})$
\mathcal{O}^-	$-\mathbf{R}(\mathbf{e}_3; \frac{\pi}{2}), \mathbf{P}_{\mathbf{e}_2 - \mathbf{e}_3}$

Table A1. The set of group generators used to construct matrix representation for each symmetry class.

315 **Type I subgroups**

System	Hermann-Maugin	Schonflies	Group	Nature
Triclinic	1	Z_1	$\mathbf{1}$	$\overline{\text{ICP}}$
Monoclinic	2	C_2	Z_2	$\overline{\text{ICP}}$
Orthotropic	222	D_2	D_2	$\overline{\text{ICP}}$
Trigonal	3	C_3	Z_3	$\overline{\text{ICP}}$
Trigonal	32	D_3	D_3	$\overline{\text{ICP}}$
Tetragonal	4	C_4	Z_4	$\overline{\text{ICP}}$
Tetragonal	422	D_4	D_4	$\overline{\text{ICP}}$
Hexagonal	6	C_6	Z_6	$\overline{\text{ICP}}$
Hexagonal	622	D_6	D_6	$\overline{\text{ICP}}$
	∞	C_∞	$\text{SO}(2)$	$\overline{\text{ICP}}$
	$\infty 2$	D_∞	$\text{O}(2)$	$\overline{\text{ICP}}$
Cubic	23	T	\mathcal{T}	$\overline{\text{ICP}}$
Cubic	432	O	\mathcal{O}	$\overline{\text{ICP}}$
	532	I	\mathcal{I}	$\overline{\text{ICP}}$
	$\infty\infty$		$\text{SO}(3)$	$\overline{\text{ICP}}$

Table A2. Dictionary between different group notations for Type I subgroups. The last column indicates the nature of the group: C = Chiral, P= Polar, I = Centrosymmetric, and overline indicates that the property is missing.

316 **Type II subgroups**

System	Hermann-Maugin	Schonflies	Group	Nature
Triclinic	$\bar{1}$	C_i	Z_2^c	$\overline{\text{ICP}}$
Monoclinic	$2/m$	C_{2h}	$Z_2 \oplus Z_2^c$	$\overline{\text{ICP}}$
Orthotropic	mmm	D_{2h}	$D_2 \oplus Z_2^c$	$\overline{\text{ICP}}$
Trigona	$\bar{3}$	S_6, Z_{3i}	$Z_3 \oplus Z_2^c$	$\overline{\text{ICP}}$
Trigonal	$\bar{3}m$	D_{3d}	$D_3 \oplus Z_2^c$	$\overline{\text{ICP}}$
Tetragonal	$4/m$	C_{4h}	$Z_4 \oplus Z_2^c$	$\overline{\text{ICP}}$
Tetragonal	$4/mmm$	D_{4h}	$D_4 \oplus Z_2^c$	$\overline{\text{ICP}}$
Hexagonal	$6/m$	C_{6h}	$Z_6 \oplus Z_2^c$	$\overline{\text{ICP}}$
Hexagonal	$6/mmm$	D_{6h}	$D_6 \oplus Z_2^c$	$\overline{\text{ICP}}$
	∞/m	$C_{\infty h}$	$\text{SO}(2) \oplus Z_2^c$	$\overline{\text{ICP}}$
	∞/mmm	$D_{\infty h}$	$\text{O}(2) \oplus Z_2^c$	$\overline{\text{ICP}}$
Cubic	$m\bar{3}$	T_h	$\mathcal{T} \oplus Z_2^c$	$\overline{\text{ICP}}$
Cubic	$m\bar{3}m$	O_h	$\mathcal{O} \oplus Z_2^c$	$\overline{\text{ICP}}$
	$\bar{5}3m$	I_h	$\mathcal{I} \oplus Z_2^c$	$\overline{\text{ICP}}$
	$\infty/m\infty/m$		$\text{O}(3)$	

Table A3. Dictionary between different group notations for Type II subgroups. The last column indicates the nature of the group: C = Chiral, P= Polar, I = Centrosymmetric, and overline indicates that the property is missing.

317 **Type III subgroups**

System	Hermann-Maugin	Schonflies	Group	Nature
Monocinic	m	C_s	Z_2^-	$\overline{\text{ICP}}$
Orthotropic	$2mm$	C_{2v}	D_2^v	$\overline{\text{ICP}}$
Trigonal	$3m$	C_{3v}	D_3^v	$\overline{\text{ICP}}$
Tetragonal	$\bar{4}$	S_4	Z_4^-	$\overline{\text{ICP}}$
Tetragonal	$4mm$	C_{4v}	D_4^v	$\overline{\text{ICP}}$
Tetragonal	$\bar{4}2m$	D_{2d}	D_4^h	$\overline{\text{ICP}}$
Hexagonal	$\bar{6}$	C_{3h}	Z_6^-	$\overline{\text{ICP}}$
Hexagonal	$6mm$	C_{6v}	D_6^v	$\overline{\text{ICP}}$
Hexagonal	$\bar{6}2m$	D_{3h}	D_6^h	$\overline{\text{ICP}}$
Cubic	$\bar{4}3m$	T_d	O^-	$\overline{\text{ICP}}$
	∞m	$C_{\infty v}$	$O(2)^-$	$\overline{\text{ICP}}$

Table A4. Dictionary between different group notations for Type III subgroups. The last column indicates the nature of the group: C = Chiral, P=Polar, I = Centrosymmetric, and overline indicates that the property is missing.

318 **Appendix B Generators of space group #214**

Consider the affine space \mathcal{E}^3 , the vector space \mathbb{R}^3 acts on \mathcal{E}^3 by translations. The affine group $\text{Aff}(\mathcal{E}^3)$ of \mathcal{E}^3 , which is the set of all affine invertible transformations is constructed as the semidirect product of \mathbb{R}^3 by $\text{GL}(3)$, the general linear group of \mathbb{R}^3

$$\text{Aff}(\mathcal{E}^3) = \text{GL}(\mathbb{R}^3) \rtimes \mathbb{R}^3$$

as such, an affine transformation is given by a pair $(\mathbf{Q}, \mathbf{v}) \in \text{GL}(\mathbb{R}^3) \times \mathbb{R}^3$. Composition of transformations follows from the construction of $\text{Aff}(\mathcal{E}^3)$ as a semi-direct product, to be explicit:

$$(\mathbf{Q}_2, \mathbf{v}_2) \odot (\mathbf{Q}_1, \mathbf{v}_1) = (\mathbf{Q}_2 \mathbf{Q}_1, \mathbf{Q}_2 \mathbf{v}_1 + \mathbf{v}_2)$$

Elements of $\text{Aff}(\mathcal{E}^3)$ can be nicely represented by (4x4) block matrices:

$$\left(\begin{array}{c|c} \mathbf{Q} & \mathbf{v} \\ \hline 0 & 1 \end{array} \right)$$

319 the internal law in $\text{Aff}(\mathcal{E}^3)$ following the matrix product in $\mathbb{M}_{4,4}$.

For our needs, we are interested not in the full affine group but in the group of isometries of \mathcal{E}^3 , this group $\text{Euc}(\mathcal{E}^3)$ is a subgroup of $\text{Aff}(\mathcal{E}^3)$ and defined as the semi direct product of the orthogonal group and the spatial translation of \mathbb{R}^3

$$\text{Euc}(\mathcal{E}^3) = \text{O}(\mathbb{R}^3) \rtimes \mathbb{R}^3$$

320 Space groups can be considered as discrete subgroups of $\text{Euc}(\mathcal{E}^3)$.

321 The generators of the space group $I4_132$ (No. 214) are given in the following table in various
322 notations [55]:

Seitz	Math	Matrices in conventional basis \mathcal{B}
$\{2_{001} 1/2\ 0\ 1/2\}$	$(\mathbf{R}(\pi, \mathbf{e}_3); \frac{1}{2}(\mathbf{e}_1 + \mathbf{e}_3))$	$\begin{bmatrix} -1 & 0 & 0 & 1/2 \\ 0 & -1 & 0 & 0 \\ 0 & 0 & 1 & 1/2 \\ 0 & 0 & 0 & 1 \end{bmatrix}_{\mathcal{B}}$
$\{2_{010} 0\ 1/2\ 1/2\}$	$(\mathbf{R}(\pi, \mathbf{e}_2); \frac{1}{2}(\mathbf{e}_2 + \mathbf{e}_3))$	$\begin{bmatrix} -1 & 0 & 0 & 0 \\ 0 & 1 & 0 & 1/2 \\ 0 & 0 & -1 & 1/2 \\ 0 & 0 & 0 & 1 \end{bmatrix}_{\mathcal{B}}$
$\{3_{111}^+ 0\}$	$(\mathbf{R}(\frac{2\pi}{3}; \mathbf{e}_1 + \mathbf{e}_2 + \mathbf{e}_3), \underline{0})$	$\begin{bmatrix} 0 & 0 & 1 & 0 \\ 1 & 0 & 0 & 0 \\ 0 & 1 & 0 & 0 \\ 0 & 0 & 0 & 1 \end{bmatrix}_{\mathcal{B}}$
$\{2_{110} 3/4\ 1/4\ 1/4\}$	$(\mathbf{R}(\pi, \mathbf{e}_1 + \mathbf{e}_2); \frac{1}{4}(3\mathbf{e}_1 + \mathbf{e}_2 + \mathbf{e}_3))$	$\begin{bmatrix} 0 & 1 & 0 & 3/4 \\ 1 & 0 & 0 & 1/4 \\ 0 & 0 & -1 & 1/4 \\ 0 & 0 & 0 & 1 \end{bmatrix}_{\mathcal{B}}$
$\{1 1/2\ 1/2\ 1/2\}$	$(\text{Id}; \frac{1}{2}(\mathbf{e}_1 + \mathbf{e}_2 + \mathbf{e}_3))$	$\begin{bmatrix} 1 & 0 & 0 & 1/2 \\ 0 & 1 & 0 & 1/2 \\ 0 & 0 & 1 & 1/2 \\ 0 & 0 & 0 & 1 \end{bmatrix}_{\mathcal{B}}$

Table A5. Generators of the Group $I4_132$ (No. 214)

323 Appendix C Proof

324 The gyroid lattice is defined from an implicit equation (Equation 1) that creates a periodic surface.
 325 For a given value of parameter $b (= \sqrt{2})$, this surface is found to become singular, thus creating an
 326 unrealistic discontinuous solid. This section presents an explanation for the admissible variation range
 327 of gyroid parameter: $|b| < \sqrt{2}$.

328
 329 Let us first restrict the variation range of variables x, y, z in Equation 2 to $[0, 1/2]$ in order to work
 330 in the fundamental domain of function ϕ . The gyroid lattice restricted to this domain is presented in
 331 Figure A1 a).

332 The fundamental domain of the gyroid is invariant with respect to the following symmetry operations:

333 - Rotation of angle $2\pi/3$ along the axis defined by equations $y = z = x$, plotted in plain line in
 334 Figure A1 and corresponding to the transformation $(x, y, z) \rightarrow (y, z, x)$. The directing vector of
 335 this axis is $(1, 1, 1)$ in orthonormal basis \mathcal{B} and it passes through point $(0, 0, 0)$.

336 - Three rotations of angle π about the three axes defined by equations $\{y = 1/4 - x, z = 1/8\}$,
 337 $\{z = 1/4 - x, y = 1/8\}$ and $\{z = 1/4 - y, x = 1/8\}$ and plotted in dashed lines in
 338 Figure A1. These axes correspond to transformations $(x, y, z) \rightarrow (1/4 - y, 1/4 - x, 1/4 - z)$,
 339 $(x, y, z) \rightarrow (1/4 - z, 1/4 - y, 1/4 - x)$, $(x, y, z) \rightarrow (1/4 - x, 1/4 - z, 1/4 - y)$, respectively. The

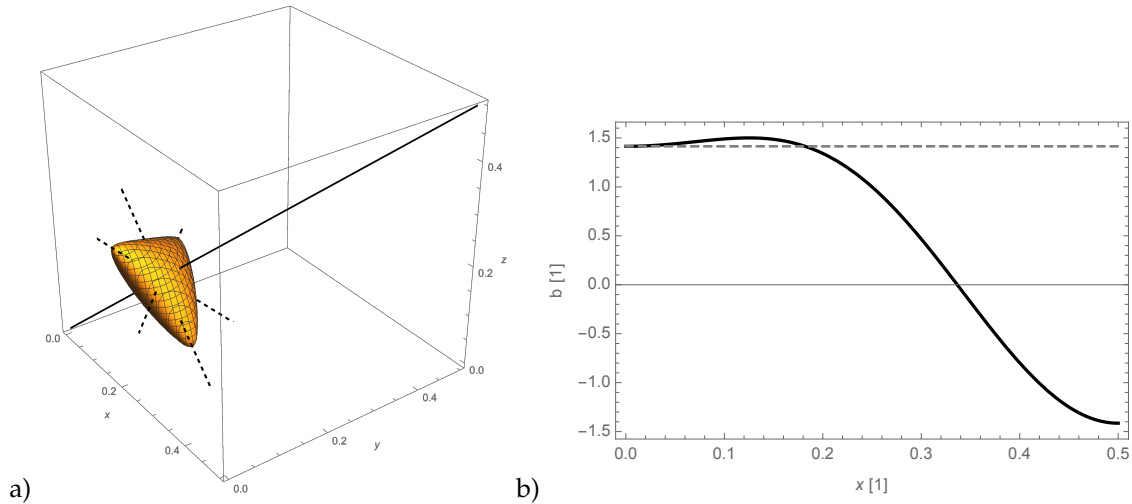


Figure A1. (a) The gyroid restricted to its fundamental domain along with symmetry axes C_3 (plain) and C_2 (dashed) ; (b) Evolution of parameter b as a function of x position along \mathbf{e}_1 axis, dashed line corresponds to $b = \sqrt{2}$

340 directing vector of these axes are, in orthonormal basis \mathcal{B} , $(1, -1, 0)$, $(1, 0, -1)$ and $(0, 1, -1)$ and
 341 they pass through points $(0, 1/4, 1/8)$, $(0, 1/8, 1/4)$ and $(1/8, 0, 1/4)$, respectively.

342 It is trivial to see that these transformations leave Equation 2 unchanged thus defining symmetry
 343 operations. As a consequence, the point symmetry group of the fundamental domain of the gyroid
 344 is conjugated to D_3 . For the sake of simplicity, we will only consider generating operations of $2\pi/3$
 345 rotation about (x, x, x) axis and π rotation about $(x, 1/4 - x, 1/8)$ axis, denoted C_3 and C_2 in the
 346 following, respectively ; the two other π rotations being generated by combination of these two
 347 generators.

348
 349 If the gyroid surface intersects one of the rotation axes non-orthogonally, then the surface
 350 automatically becomes degenerate. The expression of the normal director to the gyroid surface
 351 at its intersection point with generating symmetry axes and the equation defining this intersection
 352 point are summarized in the following Table A6:

Sym. axis & directing vector	normal to the gyroid surface	intersection point
$C_3 (1, 1, 1)_{\mathcal{B}}$	$(\cos^2 2\pi x - \sin^2 2\pi x) (1, 1, 1)_{\mathcal{B}}$	(x, x, x) with $3 \cos 2\pi x \sin 2\pi x = b$
$C_2 (1, -1, 0)_{\mathcal{B}}$	$\sin 2\pi x (\sqrt{2}/2 - \cos 2\pi x) (1, -1, 0)_{\mathcal{B}}$	$(x, -x, 0)$ with $\sqrt{2} \cos 2\pi x + \sin^2 2\pi x = b$

Table A6. The expression of the normal director to the gyroid surface at the intersection point with its symmetry axes and expression of this intersection point.

353
 354 Note that the normal director to the gyroid surface depends on variable x which, itself, is
 355 determined by parameter b through the non-linear equation defining the intersection point at which
 356 the normal director is computed.

357 One can easily check that the normal directors are generically colinear with directing vectors of C_3 and
 358 C_2 operations. However, for given values of variable x (or equivalently of parameter b), the normal to
 359 the gyroid surface is null, thus leading to singularity of the gyroid surface. These values are $x = 0 -$
 360 and thus $b = \sqrt{2}$ – leading to singularity of the gyroid surface at its intersection with axis C_2 and
 361 $x = 1/8 -$ and thus $b = 3/2$ – leading to singularity of the gyroid surface at its intersection with both axes.

362

363 Finally, the equation defining the intersection point between the gyroid surface and the C_2 axis
364 (see Figure A1 b) depends on x and parameter b : $\sqrt{2} \cos x + \sin x^2 - b = 0$. By plotting this equation
365 considering b as a function of x , we can see that there are two intersection points between the gyroid
366 surface and the C_2 axis for values of b over $\sqrt{2}$ thus showing that the gyroid surface forms a closed
367 domain in these directions leading to an unrealistic discontinuous solid.

368 References

- 369 1. Schaedler, T.A.; Carter, W.B. Architected Cellular Materials. *Annual Review of Materials Research* **2016**,
370 *46*, 187–210. doi:10.1146/annurev-matsci-070115-031624.
- 371 2. Ashby, M.; Bréchet, Y. Designing hybrid materials. *Acta materialia* **2003**, *51*, 5801–5821.
- 372 3. Fratzl, P.; Weinkamer, R. Nature's hierarchical materials. *Progress in materials Science* **2007**, *52*, 1263–1334.
- 373 4. Estrin, Y.; Bréchet, Y.; Dunlop, J.; Fratzl, P. *Architected Materials in Nature and Engineering*; Springer, 2019.
- 374 5. Hales, T.C. The Honeycomb Conjecture. *Discrete & Computational Geometry* **2001**, *25*, 1 – 22.
375 doi:10.1007/s004540010071.
- 376 6. Dolan, J.A.; Wilts, B.D.; Vignolini, S.; Baumberg, J.J.; Steiner, U.; Wilkinson, T.D. Optical Properties of
377 Gyroid Structured Materials: From Photonic Crystals to Metamaterials. *Advanced Optical Materials* **2015**,
378 *3*, 12 – 32. doi:10.1002/adom.201400333.
- 379 7. Wilts, B.D.; Michielsen, K.; Raedt, H.D.; Stavenga, D.G. Iridescence and spectral filtering of the
380 gyroid-type photonic crystals in *Parides sesostris* wing scales. *Interface Focus* **2012**, *2*, 681 – 687.
381 doi:10.1098/rsfs.2011.0082.
- 382 8. Boutin, C.; Auriault, J. Rayleigh scattering in elastic composite materials. *International Journal of Engineering*
383 *Science* **1993**, *31*, 1669–1689.
- 384 9. Parnell, W.; Abrahams, I. Homogenization for wave propagation in periodic fibre-reinforced media with
385 complex microstructure. i—theory. *Journal of the Mechanics and Physics of Solids* **2008**, *56*, 2521–2540.
- 386 10. Nassar, H.; He, Q.C.; Auffray, N. Willis elastodynamic homogenization theory revisited for periodic media.
387 *Journal of the Mechanics and Physics of Solids* **2015**, *77*, 158–178.
- 388 11. Hermann, C. Tensoren und Kristallsymmetrie. *Zs. Kristallogr* **1934**.
- 389 12. Olive, M.; Auffray, N. Symmetry classes for even-order tensors. *Mathematics and Mechanics of Complex*
390 *Systems* **2013**, *1*, 177 – 210. doi:10.2140/memocs.2013.1.177.
- 391 13. Olive, M.; Auffray, N. Symmetry classes for odd-order tensors. *ZAMM - Journal of Applied*
392 *Mathematics and Mechanics / Zeitschrift für Angewandte Mathematik und Mechanik* **2014**, *94*, 421 – 447.
393 doi:10.1002/zamm.201200225.
- 394 14. DiVincenzo, D.P. Dispersive corrections to continuum elastic theory in cubic crystals. *Physical Review B*
395 **1986**, *34*, 5450 – 5465. doi:10.1103/physrevb.34.5450.
- 396 15. Auffray, N.; Dirrenberger, J.; Rosi, G. A complete description of bi-dimensional anisotropic strain-gradient
397 elasticity. *International Journal of Solids and Structures* **2015**, *69-70*, 195 – 206. doi:10.1016/j.jisols.2015.04.036.
- 398 16. Rosi, G.; Auffray, N. Anisotropic and dispersive wave propagation within strain-gradient framework.
399 *Wave Motion* **2016**, *63 IS -*, 120 – 134.
- 400 17. Eremeyev, V.A. On the material symmetry group for micromorphic media with applications to granular
401 materials. *Mechanics Research Communications* **2018**, *94*, 8–12. doi:10.1016/j.mechrescom.2018.08.017.
- 402 18. Eremeyev, V.A.; Rosi, G.; Naili, S. Comparison of anti-plane surface waves in strain-gradient materials
403 and materials with surface stresses. *Mathematics and Mechanics of Solids* **2018**, *24*, 108128651876996.
404 doi:10.1177/1081286518769960.
- 405 19. Eremeyev, V.A.; Rosi, G.; Naili, S. Transverse surface waves on a cylindrical surface with coating.
406 *International Journal of Engineering Science* **2019**, p. 103188. doi:10.1016/j.ijengsci.2019.103188.
- 407 20. Arago, F. *Mémoire sur une modification remarquable qu'éprouvent les rayons lumineux dans leur passage à travers*
408 *certaines corps diaphanes et sur quelques autres nouveaux phénomènes d'optique*; Vol. 1, Institut National de
409 France, 1811; pp. 93–134.
- 410 21. Portigal, D.L.; Burstein, E. Acoustical Activity and Other First-Order Spatial Dispersion Effects in Crystals.
411 *Physical Review* **1968**, *170*, 673 – 678. doi:10.1103/physrev.170.673.
- 412 22. Sivardière, J. *Description de la symétrie*; EDP, 2004.

- 413 23. Auffray, N.; He, Q.C.; Le Quang, H. Complete symmetry classification and compact matrix representations
414 for 3D strain gradient elasticity. *International Journal of Solids and Structures* **2019**, *159*, 197–210.
- 415 24. Prall, D.; Lakes, R.S. Properties of a chiral honeycomb with a Poisson's ratio of -1 . *International journal of*
416 *mechanical sciences* **1997**.
- 417 25. Lakes, R. Elastic and viscoelastic behavior of chiral materials. *International journal of mechanical sciences*
418 **2001**, *43*, 1579 – 1589. doi:10.1016/s0020-7403(00)00100-4.
- 419 26. Spadoni, A.; Ruzzene, M.; Gonella, S.; Scarpa, F. Phononic properties of hexagonal chiral lattices. *Wave*
420 *Motion* **2009**, *46*, 435 – 450. doi:10.1016/j.wavemoti.2009.04.002.
- 421 27. Liu, X.N.; Hu, G.K.; Sun, C.T.; Huang, G.L. Wave propagation characterization and design of
422 two-dimensional elastic chiral metamaterial. *Journal of Sound and Vibration* **2011**, *330*, 2536–2553.
423 doi:10.1016/j.jsv.2010.12.014.
- 424 28. Liu, X.N.; Huang, G.L.; Hu, G.K. Chiral effect in plane isotropic micropolar elasticity and its
425 application to chiral lattices. *Journal of the Mechanics and Physics of Solids* **2012**, *60*, 1907 – 1921.
426 doi:10.1016/j.jmps.2012.06.008.
- 427 29. Dirrenberger, J.; Forest, S.; Jeulin, D. Effective elastic properties of auxetic microstructures: anisotropy and
428 structural applications. *International Journal of Mechanics and Materials in Design* **2013**, *9*, 21–33.
- 429 30. Bacigalupo, A.; Gambarotta, L. Homogenization of periodic hexa- and tetrachiral cellular solids. *Composite*
430 *Structures* **2014**, *116*, 461–476.
- 431 31. Fernandez-Corbaton, I.; Rockstuhl, C.; Ziemke, P.; Gumbsch, P.; Albiez, A.; Schwaiger, R.; Frenzel, T.;
432 Kadic, M.; Wegener, M. New Twists of 3D Chiral Metamaterials. *Advanced materials (Deerfield Beach, Fla.)*
433 **2019**, *31*, e1807742. doi:10.1002/adma.201807742.
- 434 32. Chen, Y.; Frenzel, T.; Guenneau, S.; Kadic, M.; Wegener, M. Mapping acoustical activity in 3D chiral
435 mechanical metamaterials onto micropolar continuum elasticity. *Journal of the Mechanics and Physics of*
436 *Solids* **2020**, p. 103877. doi:10.1016/j.jmps.2020.103877.
- 437 33. Ziemke, P.; Frenzel, T.; Wegener, M.; Gumbsch, P. Tailoring the characteristic length scale of 3D chiral
438 mechanical metamaterials. *Extreme Mechanics Letters* **2019**, *32*, 100553. doi:10.1016/j.eml.2019.100553.
- 439 34. Chen, Y.; Frenzel, T.; Guenneau, S.; Kadic, M.; Wegener, M. Mapping acoustical activity in 3D chiral
440 mechanical metamaterials onto micropolar continuum elasticity. *Journal of the Mechanics and Physics of*
441 *Solids* **2020**, p. 103877. doi:10.1016/j.jmps.2020.103877.
- 442 35. Chen, Y.; Yao, H.; Wang, L. Acoustic band gaps of three-dimensional periodic polymer cellular solids with
443 cubic symmetry. *Journal of Applied Physics* **2013**, *114*, 043521. doi:10.1063/1.4817168.
- 444 36. Rammohan, A.V.; Lee, T.; Tan, V.B.C. A Novel Morphological Model of Trabecular Bone Based on the
445 Gyroid. *International Journal of Applied Mechanics* **2015**, *07*, 1550048 – 18. doi:10.1142/s1758825115500489.
- 446 37. Ma, S.; Tang, Q.; Feng, Q.; Song, J.; Han, X.; Guo, F. Mechanical behaviours and mass transport properties
447 of bone-mimicking scaffolds consisted of gyroid structures manufactured using selective laser melting.
448 *Journal of the Mechanical Behavior of Biomedical Materials* **2019**, *93*, 158 – 169. doi:10.1016/j.jmbbm.2019.01.023.
- 449 38. Poncelet, M.; Somera, A.; Morel, C.; Jailin, C.; Auffray, N. An experimental evidence of the failure of Cauchy
450 elasticity for the overall modeling of a non-centro-symmetric lattice under static loading. *International*
451 *Journal of Solids and Structures* **2018**, *147*, 223–237. doi:10.1016/j.ijsolstr.2018.05.028.
- 452 39. Abdoul-Anziz, H.; Seppecher, P.; Bellis, C. Homogenization of frame lattices leading to second gradient
453 models coupling classical strain and strain-gradient terms. *Mathematics and Mechanics of Solids* **2019**,
454 *24*, 3976–3999.
- 455 40. Yvonnet, J.; Auffray, N.; Monchiet, V. Computational second-order homogenization of materials with
456 effective anisotropic strain-gradient behavior. *International Journal of Solids and Structures* **2020**.
- 457 41. Schoen, A.H. Infinite periodic minimal surfaces without self-intersections. *Nasa Technical Notes* **1970**, *TN*
458 *D-5541*.
- 459 42. Schoen, A.H. Reflections concerning triply-periodic minimal surfaces. *Interface Focus* **2012**, *2*, 658–668.
460 doi:10.1098/rsfs.2012.0023.
- 461 43. Dacorogna, B. *Introduction to the Calculus of Variations*; World Scientific Publishing Company, 2014.
- 462 44. Wohlgemuth, M.; Yufa, N.; Hoffman, J.; Thomas, E.L. Triply periodic bicontinuous cubic microdomain
463 morphologies by symmetries. *Macromolecules* **2001**, *34*, 6083 – 6089. doi:10.1021/ma0019499.
- 464 45. Golubitsky, M.; Stewart, I.; Schaeffer, D.G. *Singularities and Groups in Bifurcation Theory*; Vol. 69, *Applied*
465 *Mathematical Sciences*, Springer New York: New York, NY, 1988. doi:10.1007/978-1-4612-4574-2.

- 466 46. Hahn, T.; Shmueli, U.; Wilson, A.J.C.; Prince, E. *International tables for crystallography*; D. Reidel Publishing
467 Company, 2005.
- 468 47. Craster, R.V.; Antonakakis, T.; Makwana, M.; Guenneau, S. Dangers of using the edges of the Brillouin
469 zone. *Physical Review B* **2012**, *86*, 115130. doi:10.1103/physrevb.86.115130.
- 470 48. Gazalet, J.; Dupont, S.; Kastelik, J.C.; Rolland, Q.; Djafari-Rouhani, B. A tutorial survey on waves
471 propagating in periodic media: Electronic, photonic and phononic crystals. Perception of the Bloch
472 theorem in both real and Fourier domains. *Wave Motion* **2013**, *50*, 619–654.
- 473 49. Achenbach, J. *Wave Propagation in Elastic Solids*; Elsevier, Elsevier, 1984.
- 474 50. Zakharenko, A.A. On cubic crystal anisotropy for waves with Rayleigh-wave polarization. *Nondestructive
475 Testing and Evaluation* **2006**, *21*, 61–77. doi:10.1080/10589750600779704.
- 476 51. Rosi, G.; Nguyen, V.H.; Naili, S. Surface waves at the interface between an inviscid fluid and a dipolar
477 gradient solid. *Wave Motion* **2015**, *53*, 51–65. doi:10.1016/j.wavemoti.2014.11.004.
- 478 52. Gourgiotis, P.A.; Georgiadis, H.G.; Neocleous, I. On the reflection of waves in half-spaces of
479 microstructured materials governed by dipolar gradient elasticity. *Wave Motion* **2013**, *50*, 437–455.
480 doi:10.1016/j.wavemoti.2012.10.004.
- 481 53. Mandel, J. Généralisation de la théorie de plasticité de WT Koiter. *International Journal of Solids and
482 structures* **1965**, *1*, 273–295.
- 483 54. Forte, S.; Vianello, M. Symmetry classes for elasticity tensors. *J. Elast.* **1996**, *43*, 81–108.
484 doi:10.1007/BF00042505.
- 485 55. Aroyo, M.I.; Perez-Mato, J.M.; Capillas, C.; Kroumova, E.; Ivantchev, S.; Madariaga, G. and Kirov, A.;
486 Wondratschek, H. Bilbao Crystallographic Server: I. Databases and crystallographic computing programs.
487 *Zeitschrift für Kristallographie-Crystalline Materials* **2006**, *221*, 15–27.